PROCEEDINGS, Thirty-Sixth Workshop on Geothermal Reservoir Engineering
Stanford University, Stanford, California, January 31 - February 2, 2011
SGP-TR-191

CHARACTERIZATION OF ROCK PORE FEATURES IN GEOTHERMAL SYSTEMS USING SMALL ANGLE NEUTRON SCATTERING (SANS)

Lawrence M[1]. Anovitz, Gernot Rother[1], David R. Cole[2]

[1] Chemical Sciences Division, Oak Ridge National Laboratory
MS 6110, PO 2008
Oak Ridge, Tennessee 37830, USA
e-mail: anovitzlm@ornl.gov, rotherg@ornl.gov

[2] School of Earth Sciences, Ohio State University
275 Mendenhall Laboratory, 125 South Oval Mall
Columbus, Ohio 43210, USA
e-mail: cole.618@osu.edu

ABSTRACT

Enhanced Geothermal Systems (EGS) are engineered reservoirs created to economically extract heat from low permeability and/or porosity geothermal resources. Existing geochemical reactive transport models for such systems lack essential data on the structure of the pore systems in geothermal reservoirs, and how they evolve in the relevant ranges of temperature, pressure, composition, and length scale. Small angle and ultra-small angle neutron scattering (SANS/USANS) are powerful tools to characterize the pore systems in geothermal rocks from the nano- to the micron scale. In this communication, we provide a brief summary of neutron scattering techniques, and discuss the utility of neutron scattering (NS) for EGS reservoir characterization and present example analyses of the pore systems of representative rocks from the Geysers, CA geothermal system. Future communications will address natural and experimental samples from Fenton Hill, N Mex.; Long Valley, CA, Desert Peak, NV, Yellowstone, WY and Awibengkok, Java. The results obtained by include the pore size, pore size distribution, pore number, and surface and mass fractal nature of the pore structures. Comparison of samples from the vapor-dominated and liquid dominated parts of the system show that the former has smoother,

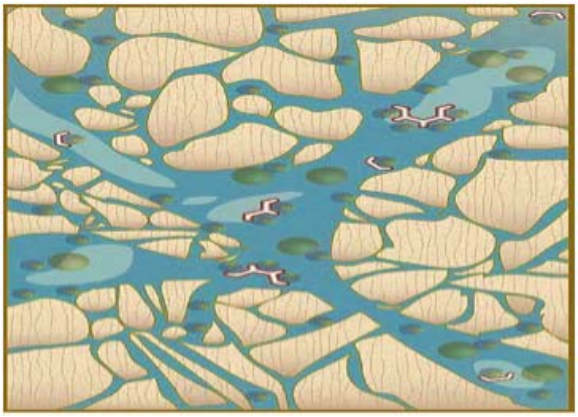

Figure 1. Schematic representation of the relationship between macroscopic flow channels and nanoenvironments (grain boundaries, pore networks) in a geothermal system (DOE, BRN. 2007).

but still fractal pore walls, and a mass fractal pore distribution not seen in the latter. In addition, the while the overall submicron porosities of the two are similar, the vapor dominated sample has a larger fraction of smaller pores. (U)SANS studies provide essential information about geothermal systems that are important for site selection, reservoir creation, stimulation, and sustained operations.

INTRODUCTION

The microstructure and evolution of pore space in subsurface rocks is a critically important factor controlling fluid flow properties in many geological formations, including the migration and retention of water, gas and hydrocarbons, sequestration

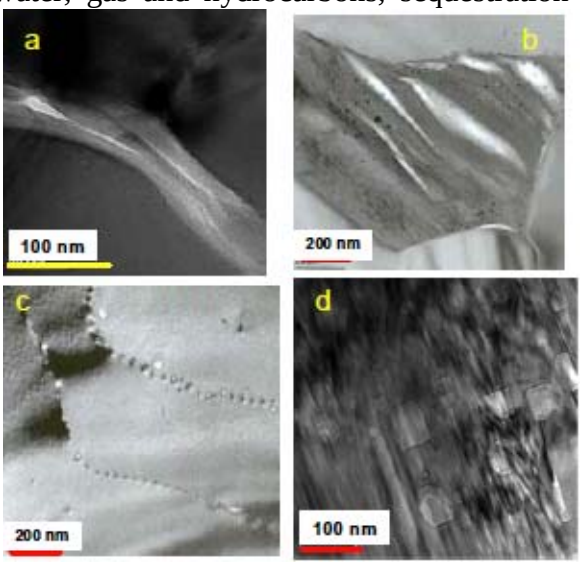

Figure 2. TEM images of porosity generation in (a) limestone, (b and c) basalt, and (d) alkali feldspar (Cole et al., 2009).

of wastes, the formation of ore deposits, and the evolution of metamorphic terranes. Fracture-dominated flow is no-doubt paramount in shallow crustal settings, but there is a continuum of coupled reaction/ transport phenomena from this scale down to the finest nanopores that influence heat- and mass-transfer in evolving geological reservoirs. As suggested schematically in Figure 1 the size, distribution and connectivity of these confined geometries collectively dictate how fluids migrate into and through these micro- and nanoenvironments, wet and react with the solid surfaces, and thus, interact with the bulk of the rock matrix. Such interactions are clearly significant with regard to water-rock chemical interactions, and may also play an important role in overall heat transfer. Differences in pore structures may control and/or be controlled by differences in the geothermal environment, as caprock vs. reservoir behavior, and high temperature, vapor-dominated vs. “normal-temperature”, liquid dominated regimes. In order to understand the history and predict the evolution of any geothermal system, therefore, its physical and chemical “fingerprints” must be deciphered, not just at the macroscale, but on the nanoscale as well.

While the importance of porosity and pore-evolution has long been recognized, the importance of nanoscale porosity has only recently been investigated. Nanoscale porosity includes cracks, grain boundaries, fluid inclusions and single pores, and networks of pores of random shapes and orientations. Nanopores may or may not interconnect with larger fluid volumes. Accessible, interconnected nanopores are arguably a critical part of the entire pore system. They act as pore throats, constraining overall flow and are the most likely local for extensive rock alteration and/or carbon sequestration and other fluid/rock reactions. In smaller pores, larger fractions of the pore fluid are in contact with the pore walls, possibly causing increased heat transfer from the rock to the fluid and, depending on the rock-fluid interactions, strong sorption effects (cf. Rother et al., 2007).

Limited attention has been paid to date to nanoporosity because the texture and overall volume of pores at the submicron scale have been difficult to characterize in a statistically meaningful manner. This is because of the wide variation in pore morphology (i.e. length scales, pore shapes, connectivity, etc.) involved. While electron microscopy can provide detailed 2D images of pores at the nanoscale (cf. Figure 2), the high magnifications needed mean that the total volume of the rock imaged is quite small. In fact, Howard and Reed (2005) calculated that all the material that had ever been studied in all of the transmission electron microscopes in the world amounts to a total of less than 1 cubic centimeter in volume.

While the statistical utility of high-resolution imaging is limited, a combination of small- and ultra-small angle neutron scattering (SANS and USANS) is well suited to a statistical characterization of pores from the nano- to the micro-scale and, with the addition of other techniques, enables a comprehensive structural characterization from the nm to cm and larger scales.

Scattering contrast in rock samples arises primarily from the difference in the coherent

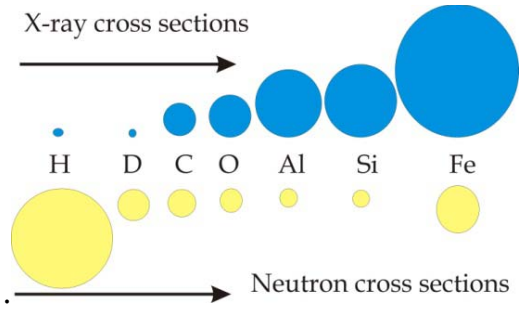

Figure 3: Comparative scattering cross-sections of X-rays and neutrons for several common elements.

scattering length densities (SLD) of the rock and the pores within it, while the SLDs of different minerals present in the rock are often similar, making their individual scattering contributions negligible. Thus, NS analysis of a rock sample provides a direct characterization of the pore structure. Neutron beam cross sections at NS instruments are typically several cm^2, and thermal neutrons are highly penetrating, compared with photons and electrons. Thus, the scattering curve results from a relatively large, and more statistically meaningful rock volume (e.g. hand-sample-size, typically approximately 30 mm^3, Anovitz et al., 2009). In addition, the high penetrating power of neutrons, relative to X-rays, allows analysis of thicker rock samples by NS.

The SLD of phase *j* is given by:

$$\rho_j^* = \sum_{i=1}^{n} b_i \frac{\rho_j N_A}{M_i} \quad (1),$$

where b_i is the bound coherent scattering length of atom *i*, *N* the total number of atoms in the molecule, ρ_j is the mass density, N_A is the Avogadro constant and M_i is the molar mass.

Unlike with X-rays, the total neutron scattering cross section for hydrogen is large (Figure 3), allowing studies of water/rock interactions at the nano- to micro-scales (and at various time scales with inelastic/ quasielastic scattering techniques). In fact, while the scattering cross section for X-rays is a function of the atomic number, that for neutrons is not (Figure 3), thus providing a significantly different, and very useful contrast. Scattering analysis sees both pores that are connected to the overall network and those that are not, this feature of neutron scattering allows us to differentiate between these two groups. Significantly, the large difference in SLD between hydrogen and deuterium means that the rock can be saturated with a contrast matched H_2O/D_2O mixture to separate connected from unconnected porosity, or with other fluids of interest to study fluid confinement.

TECHNICAL ASPECTS OF (U)SANS EXPERIMENTS

While a full discussion of the theory and practice of small angle scattering (e.g Guinier and Fournet, 1955; Hammouda, 2009; Radlinski, 2006) is outside the scope of this communication, some basic background is warranted. Neutrons for scattering experiments are generated either from the decay of ^{235}U in a nuclear reactor (e.g. High Flux Isotope Reactor at the Oak Ridge National Laboratory, HFIR/ORNL; NIST Center for Neutron Research, NCNR; Chalk River, Institut Laue-Langevin, ILL, FRM2 in Munich, BER-II at HZB Berlin, LLB Saclay, ANSTO Sidney, Hanaro facility South Korea, and others), or by spallation caused by collision of protons with a neutron-rich target (Spallation Neutron Source at ORNL, SNS/ORNL; ISIS at the Rutherford Appleton Laboratory; Los Alamos Neutron Science Center, LANSCE, SINQ at PSI Villigen, and others).

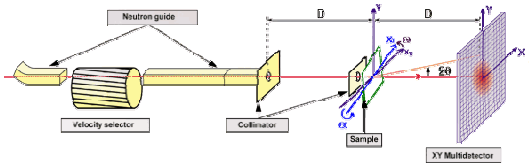

Figure 4: Schematic representation of a SANS experiment showing beam path, sample scattering and detector

Neutrons can be grouped by energy. Fission in the reactor generates fast neutrons with energies too high to use (~ 2 MeV). These are slowed down, through interaction with moderators such as heavy water, to first hot, then thermal neutrons with wavelengths of 1-4 Å and energies of 10 – 100 meV. These latter are the neutron energies used by many diffractometers and spectrometers, and also the USANS instrument at NIST. SANS instruments (installed at many neutron sources), commonly use cold neutrons to extend the Q-range of the instrument (longer wavelengths for resolution of larger spatial structures). Thermal neutrons (with a Maxwellian spectral distribution peak at 1.8 Å) are interacted with hydrogen or deuterium as a liquid in a cold source. The resultant neutrons pass down a beam tube equipped with appropriate neutron guides and shutters delivering neutrons to the SANS instrument.

The setup of a typical pinhole SANS instrument is shown schematically in Figure 4. Neutrons first pass through a velocity selector, a rotating spiral pathway that acts as a monochromator, i.e. only neutrons with a certain range of speeds (wavelengths) can pass. They then pass down a long, variable guide and collimation section. An aperture of suitable size is placed at the end of the collimator system and defines the cross section of the neutron beam interacting with the sample. The sample scatters part of the neutrons, the other fraction is transmitted or absorbed. The intensity of scattered and transmitted neutrons is measured with 1D or 2D detectors. The neutron transmission is measured for absolute intensity calibration.

The neutron detector for a SANS instrument (there are various designs)

Figure 5: Detector tanks for two SANS instruments at the HFIR. The General Purpose SANS (with tank door open) and the bioSANS (nearer). The sample positions are at the other end of the tanks (far left).

typically consists of a square plate up to a meter on a side with an array of detection pixels. This detector resides inside a large, cylindrical vacuum chamber (typically 10 – 20 m long) in order to reduce interference from scattering by molecules or particles in the air (Figure 5). The position of the detector and the beam stop in the tank can be varied to obtain data on a wider range of scattering angles. The Q ranges covered by SANS instruments vary somewhat as a function of instrument parameters, selected wavelengths and the use of focusing lenses, but are typically in the range from $1*10^{-3} < Q < 0.7$ Å^{-1}, which samples scattering features (e.g. pores) with sizes ranging from approximately 10 to 5000 Å.

The resultant scattering pattern typically looks something like that shown in Figure 6. This pattern will be radially symmetrical if

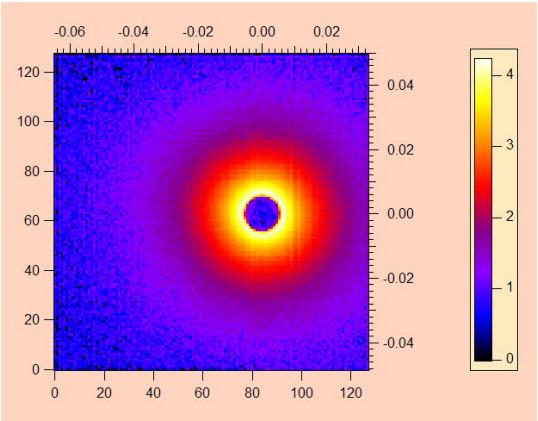

Figure 6: Example scattering data at a single detector distance. Intensities are higher near the direct beam (lower Q, larger scale lengths). Scattering is isotropic for this sample. The center is intentionally offset to increase the Q-range sampled.

there is no preferred orientation in the sample, and can then be radially integrated to obtain the scattering curve. Appropriate corrections have to be applied for detector sensitivity, sample thickness and transmission, beam intensity, background and empty cell scattering. Data are

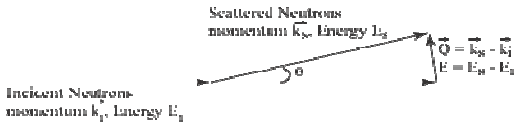

Figure 7: Vector diagram showing the origin of the Q vector.

normalized to absolute intensities by measurement of a calibration standard or by the empty beam flux method.

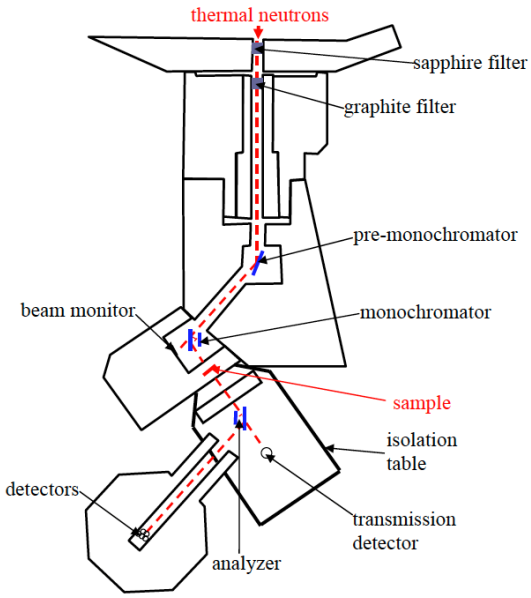

Figure 8: Schematic illustration of the USANS instrument at NIST/NCNR. (Figure from Hammouda, 2009, used with permission of the author)

While the resultant integrated and normalized intensity could be plotted in terms of scattering angle, it is more commonly shown in terms of the momentum transfer vector Q (with units of Å^{-1}), defined as shown in Figure 7, where Q is the momentum transfer, and E is the energy transfer.

The USANS instrument uses an entirely different design in order to measure scattering at lower Q-values than those obtained by SANS. The USANS at NIST/NCNR covers a Q range from $4*10^{-5}$ $Å^{-1} < Q < 0.01$ $Å^{-1}$, which corresponds to a size range of 7.8 μm > d > 628 Å (Hammouda, 2009). Thus, the two techniques are complementary. The USANS uses thermal wavelength neutrons (2.4 Å) and the Bonse-Hart method in which neutrons are first monochromated by a triple-bounce, channel-cut single-crystal silicon monochromator, then pass through the sample to another similar monochromator (the analyzer) and then to a detector. Scanning the analyzer permits measurement of the angular dependence of the scattering intensity. The use of these paired monochromators allows very narrow wavelength resolution ($\Delta\lambda/\lambda = 0.059$), but the beam intensity is low relative to the SANS, making count times longer. In addition, the use of a slit, rather than a pinhole geometry requires desmearing of the resultant USANS scattering pattern.

It should be noted that, in many cases, even the combination of SANS and USANS does not cover a sufficiently large Q range to describe the complete scattering curve for many rocks. There are several approaches to filling this gap, including backscattered electron (BSE) imaging (Radlinski et al., 2004, Anovitz et al., in prep.), small angle light scattering (SALS, cf. Cipelletti and Weitz, 1999), and spin-echo SANS (SESANS, cf. Bouwman et al., 2000), but these will not be discussed further here.

Total neutron scattering is characterized by coherent and incoherent contributions. Coherent scattering is Q dependent, and contains the information about scattering structures, whereas incoherent scattering is Q independent. For (U)SANS analysis incoherent scattering, largely due to the hydrogen content of the sample, results in a background that limits the ability to obtain quality information at high-Q. For NS data analysis the incoherent background needs to be subtracted from the scattering curve. This limitation can often be overcome by exchanging deuterium, which has a much lower incoherent scattering cross section, for hydrogen in the sample.

The coherent signal is the scattering intensity I(Q), with

$$Q = 4\pi \sin\frac{\theta}{\lambda} \qquad (2),$$

the momentum transfer, where 2θ is the scattering angle and λ the wavelength of the neutrons. The scattering data can be analyzed in reciprocal space by least-square fitting to model functions or in real space after Fourier-transformation. Both techniques yield information about the shape and size or size ranges of scatterers. The invariant Z, defined by

$$Z = \int_0^\infty Q^2 I(Q) dQ \qquad (3),$$

yields direct, model-independent information about the scattering contrast and volume of scatterers. For a two-phase system the invariant is given by:

Figure 9: Example of eight samples from different geothermal fields ground to 150 microns sample thickness on quartz glass plates.

$$Z = 2\pi^2 \phi_1 (1-\phi_1)(\rho_1^* - \rho_2^*)^2 \quad (4),$$

with ϕ_1 equal to the volume fraction of phase 1 and ρ_1 its coherent SLD.

PREPARATION OF SAMPLES

While neutrons are very penetrating, preparation of samples with a suitable thickness is important. If the sample is too thin, scattering intensity will be too low. If the sample is too thick multiple scattering will lower the scattering intensity at low Q and raise it at higher Q, distorting the signal. Thus the sample must be sufficiently thin to avoid this effect. Anovitz et al. (2009) showed that, for limestone samples, a thickness of 150 microns met both criteria.

We have tested two approaches to preparing samples of suitable thickness. It is possible to grind samples to a suitable thickness using a soluble glue to attach the rock to a glass slide and then to carefully remove the sample from the slide and remount it on a cadmium mask. We have used this approach successfully. However, samples prepared in this manner are fragile and tend to fracture during remounting, leading to smaller sample volumes and, therefore, longer measurement times.

Because of these difficulties, we tested whether samples could be measured without removing them from the glass slides. This required mounting the samples on quartz glass, rather than the standard borosilicate glass used for most thin sections, because the boron absorbs neutrons. Anovitz et al. (2009) showed that, using this approach there is very little coherent scattering from the glass itself, although the incoherent background is reached at slightly lower Q values than for the unmounted sample. The addition of a glue layer increases the coherent scattering slightly, but may also decrease the incoherent background (possibly due to increased adsorption of water vapor on the glue-free frosted glass surface). Both a permanent epoxy and superglue were tried, and there was little discernable difference between the two. Tests showed that scattering from even two quartz glass plates plus the glue was only three to four percent of that from the sample. Thus, except for a possible slight loss of information at the highest Q-values, these tests showed that samples can be measured while still mounted on quartz-glass slides, which dramatically improves the ease of sample preparation and handling. An example of such samples from several geothermal fields, mounted on cadmium masks, is shown in Figure 9.

ANALYSIS OF (U)SANS DATA

A wealth of information can be obtained about the pore structure of rocks from (U)SANS data. Again, a full discussion is beyond the scope of this paper, and readers are referred elsewhere (Radlinski 2006, Anovitz et al. 2009, in prep.).

Once the raw data have been reduced (cf. Kline, 2006), the data can be examined to determine such features as the overall porosity, cumulative porosity, pore distribution geometry (mass fractal behavior), the nature of the pore/rock interface (surface fractal behavior), and characteristic lengths associated with the fractal behavior, as well as the surface area to volume ratio. Pore or grain-size groupings may also appear as bumps or steps in the data. In appropriate cases the nature of a confined pore fluid can also be examined (Rother et al., 2007; Cole et al., 2009).

Figure 10 shows a schematic example of a scattering curve plotting the log of scattering intensity (I) in units of cm^{-1} as a function of the log of the scattering vector (Q) in units of inverse angstroms. In many samples the scattering intensity is constant as a function of Q at high Q. In this range, coherent

(structural) scattering is overwhelmed by the flat incoherent background, which is primarily a function of the hydrogen content of the sample.

The slopes of the remaining parts of the curve are determined by the surface from which scattering occurs. Slopes between -2 and -3 are characteristic of mass fractal systems (where density scales with total volume), those between -3 and -4 of surface fractal systems (where surface area scales with ruler length), and those between -4 and -5 of non-fractal "fuzzy" interfaces in which the scattering length density varies monotonically between two phases. Smooth interfaces give rise to scattering with a power-law slope of -4, which is referred to as Porod scattering. In some samples there may be some point, known as the surface fractal correlation length r, which forms the upper scaling limit of surface fractal behavior. Below this point the scaling exponent is dominated by mass fractal behavior, with a dimension (D_m) equal to the slope, which describes the pore distribution within the sample. At yet lower Q-values corresponding to length scales greater than the largest aggregates in a sample the slope of I vs. Q should flatten. This "Guinier region" is commonly not observed in our data. This implies that the maximum size of features covered by the (U)SANS measurements is smaller than the largest grain size of the rock.

Various transformations are commonly used to interpret the data. For instance, the Porod transform (plotting Q^4*I as a function of Q) removes the dominating effect of the surface scattering from the data and enhances the visibility of structural detail. Integration of the Kratky transform (Q^2I as a function of Q) yields the invariant (Z in equation 4) that, in turn, can be used to calculate the overall porosity of the sample. However, the specific techniques adopted for data analysis and fitting must be appropriate for the samples under analysis.

It would clearly also be useful to obtain pore size distributions from scattering data. With

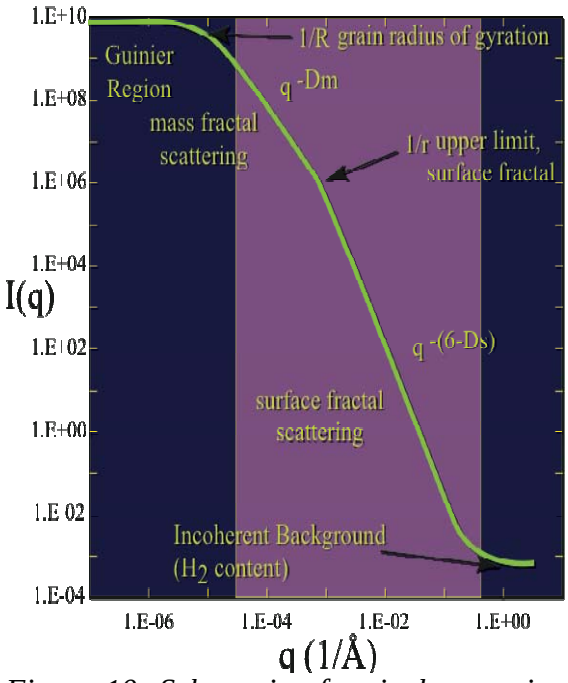

Figure 10: Schematic of typical scattering curve. The pink area shows the Q range typically reached by (U)SANS measurements.

certain limiting assumptions, several authors have suggested methods of doing so. For example, Hinde (2004) and Radlinski and co workers (e.g. Radlinski et al., 2004) have developed the polydisperse spherical pore (PDSP) model in which fractal pore shapes are treated as an assemblage of spherical pores. Maximum entropy techniques (e.g. Potton et al., 1988a,b, Morrison et al., 1992), Fourier calculations (e.g. Muller et al., 1995) and Monte Carlo approaches (e.g. Martelli and Di Nunzio, 2002) have also been applied. Many of these approaches, however, require assumptions about pore shapes, an issue made more complicated by the heterogeneous, commonly fractal shapes of rock pores (Figure 2). We have adopted a simpler approach in which we only calculate the cumulative pore volume, which makes

fewer assumptions (see Anovitz et al., in prep. for a more complete discussion).

EXAMPLE RESULTS FROM THE GEYSERS GEOTHERMAL SYSTEM

In order to test the utility of the neutron scattering approach to understanding the

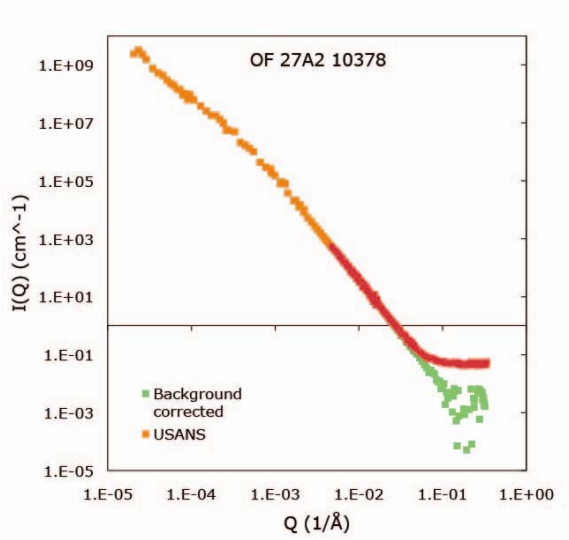

Figure 11: (U)SANS scattering data for sample from well OF 27A2 St1, 10,378 feet from The Geysers, CA.

relationship between the pore features and water (vapor)-rock interaction processes in a commercial geothermal system we selected samples from the Geysers. In particular, we focused on the NW Geysers because it has two separate reservoir zones, an isothermal upper zone (NTZ; normal temperature zone) hosted in a metagraywacke that is around 240^{o}C, and a high temperature reservoir (HTR) (from 260-360^{o}C) that is in a hornfelsic graywacke. The lower steam reservoir has a conductive thermal gradient and typically exhibits lower permeability compared to the upper NTZ. The HTR is also characterized by much higher noncondensable gas contents in the produced steam. It is of great practical importance to understand if the pore-scale characteristics of the two reservoir host rocks might have some unique differences that determine the behaviors of these two geothermal reservoirs. Results are presented from a representative rock from each zone.

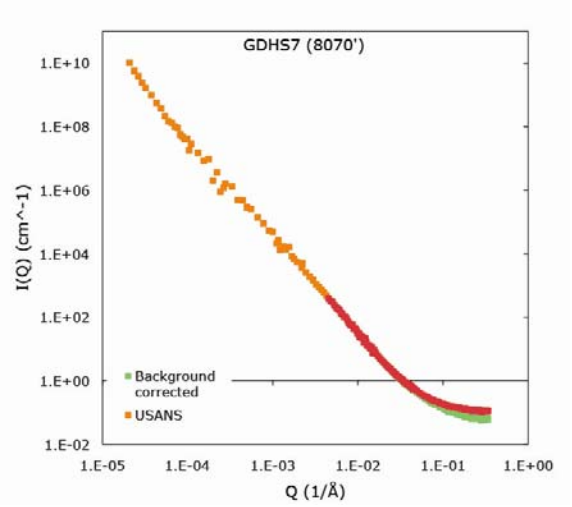

Figure 12: (U)SANS scattering data for sample from well GDHS7, 8070 feet from The Geysers, CA.

Figures 11 and 12 show the scattering data for two samples from The Geysers, one from well Ottoboni Federal 27A2 Sidetrack 1 (OF 27A2 St1) at a depth of 10,378 feet, and one from well GDHS 7 at a depth of 8070 feet. Both are metagreywackes, but OF 27A2 St1 comes from the high temperature, vapor dominated zone, while GDHS 7 comes from the normal temperature zone (Walters, pers. comm.).

Several features are apparent in these plots. First, the curves are relatively smooth, implying a relatively even distribution of pores at all sizes, and both curves have similar background levels, implying similar hydrogen contents. In neither case is a flat scattering curve observed at low Q. Thus, there is significant porosity at dimensions greater than that observable by (U)SANS and data from a third technique such as BSE, SALS or SESANS are clearly needed to complete the curve.

As mentioned above, these data can be better examined and compared by plotting them in Porod space, an approach that

normalizes the measured data to the -4 (log-log) slope expected for smooth interfaces and emphasizes the unique features of each scattering curve. This is shown for both samples in Figure 13. For instance, the data for OF 27A2 St1 show greater scattering intensity, implying higher porosity, and evidence of both surface and mass fractal behavior. Only surface fractal behavior is apparent in the sample from GDHS 7, but the pore/rock interfaces are apparently much rougher than in OF 27A2 St1. The surface fractal dimension derived from OF 27A2 St1 is ~2.4, and surface fractal behavior dominates the scattering only below a Q value of ~1E-3 $Å^{-1}$, while that of GDHS 7 is ~2.85, and dominates scattering below ~5E-5 $Å^{-1}$. This shows that the pore/grain boundaries are significantly rougher in GDHS 7 over a much larger range of pore sizes. At the largest scales observed, however, the slope of the scattering curve for the GDHS 7 becomes flat in Porod space, implying a smooth boundary at larger scale lengths. Scattering in OF 27A2 St1 is dominated at the largest length scales observed by mass fractal behavior, with a fractal dimension of ~2.2.

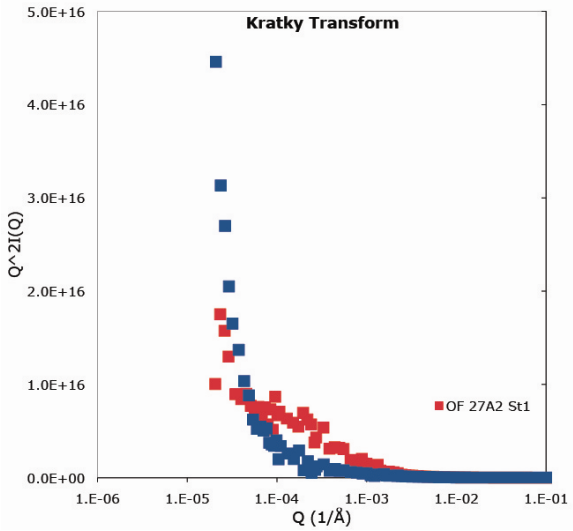

Figure 14: Kratky transforms for both samples OF 27A2 st1 at 10,378 feet and GDHS 7 at 8070 feet.

As described above, the Krakty transform (Figure 14) and the invariant provide information on the total and cumulative porosities of a sample. The utility of this approach is somewhat limited for these samples by the lack of suitable low-Q data.

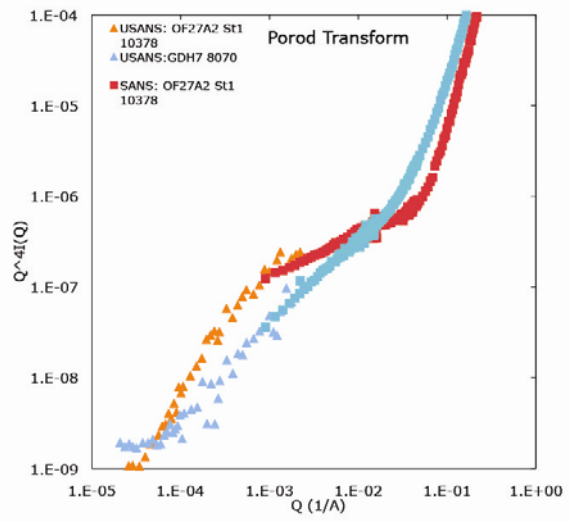

Figure 13: Porod-transformed small and ultra small angle neutron scattering data for two samples from the Geysers geothermal field

However, it is quite clear that there is significantly greater high-Q (small size) porosity in the sample from well OF 27A2 St1 in the high-temperature, vapor dominated zone compared to the sample from well GDHS 7 in the normal temperature zone, which appears to exhibit more micron-scale porosity. Overall, at the scales we were able to probe, the total porosities of the two samples were very similar. That of GDHS 7 was 0.016 and that of the OF 27A2 St1 was 0.017, but it is clear that this overall porosity is differently distributed as a function of scale. One must also remember that these porosity values are lower bounds, as the low-Q data have not been determined i.e. porosity at larger scales is neglected. Deconvolution of the entire profile to obtain a meaningful cumulative porosity awaits the availability of lower-Q data.

These analyses show that there are significant differences in the pore structure of the normal and high-temperatures zones at the Geysers, which are likely to provide important controls on the nature of, and differences in, fluid and heat transport in each.

While scattering data provide a new approach to characterization of porosity in geothermal and other geologic systems at many scales, it should be pointed out that the results are often complemented by the addition of data from other approaches. TEM images provide direct visualization of the shape and distribution of nanopores that is of great utility in interpreting the scattering results. In addition, it is likely that X-ray or neutron tomographic analyses can be used, not only to provide three dimensional pictures of the pore network, but in a manner similar to that used for BSE images to extend the scattering curves to lower Q in an even more quantitative manner. Together, these approaches provide a unique avenue for characterization of the pore and nano- to micro fracture networks that clearly play an important role in hydrothermal systems.

ACKNOWLEDGEMENTS

Research sponsored by the Geothermal Technologies Program, Office of Energy Efficiency and Renewable Energy, U.S. Department of Energy under contract DE-AC05-00OR22725, Oak Ridge National Laboratory, managed and operated by UT-Battelle, LLC. We would also like to thank Mark Walters of Calpine, and Joe Moore of the Energy and Geoscience Institute for their help both supplying samples from the Geysers, as well as understanding the associated geologic environment.

REFERENCES

Anovitz, LM, Lynn, GW, Cole, DR, Rother, G, Allard, LF JR., Hamilton, WA, Porcar, L, and Kim, MH (2009) A new approach to quantification of metamorphism using ultra-small and small angle neutron scattering. Geochim. Cosmochim. Acta 73, 7303-7324.

Anovitz, L.M., Cole, D.R., Rother, G., Valley, J.W., Allard, L.F. Jr., Jackson, A., and Littrell, K.C. (in prep.) Analysis of Macro to Nano-Porosity in the St. Peter Sandstone Using (Ultra) Small Angle Neutron Scattering and Backscattered Electron Imaging.

Bouwman, WG, van Oossanen, M, Uca, O, Kraan, WH and Rekveldt, MT (2000) Development of spin-echo small-angle neutron scattering. Journal of Applied Crystallography, 33, 767-770.

Cipelletti, L, and Weitz, DA (1999) Ultralow-angle dynamic light scattering with a charge coupled camera based multispeckle, multitau correlator. Rev. Sci, Instr. 70, 3214-3221.

Cole, DR, Mamontov, E and Rother, G (2009) Chapter 19. Structure and dynamics of fluids in microporous and mesoporous earth and engineered materials. In: *Neutron Applications in Earth, Energy, and Environmental Sciences*, L. Liang, R. Rinaldi and H. Schober, editors, Springer, 547-570.

Department of Energy (2007) Basic Research Needs for Geosciences: Facilitating 21st Century Energy Systems. 287pp.

Guinier, A and Fournet, G (1955). Small Angle Scattering of X-rays. New York: John Wiley.

Hammouda, B (2009) Probing Nanoscale Structures. The SANS Toolbox, book

available online at **Error! Hyperlink reference not valid.**

Hinde, AL (2004) PRINSAS – a Windows-based computer program for processing and interpretation of small-angle scattering data tailored to the analysis of sedimentary rocks. J. Appl. Cryst. 37, 1020-1024.

Howard CV and Reed MG (2005) Unbiased Stereology (Garland Science/BIOS Scientific, New York).

Kline, SR (2006), "Reduction and analysis of SANS and USANS data using IGOR Pro," Journal of Applied Crystallography, **39** 895-900.

Martelli, S and Di Nunzio, PE (2002) Particle size distribution of nanospheres by Monte Carlo fitting of small angle X-ray scattering curves. Particle and Particle Systems Characterization 19, 247-255.

Morrison, JD, Corcoran, JD and Lewis, KE (1992) The determination of particle-size distributions in small-angle scattering using the maximum-entropy method. Journal of Applied Crystallography, 25, 504-513.

Muller, JJ, Hansen, S, Lukowski, G, and Gast, K et al., 1995 Multimodal particle-size distribution or fractal surface of acrylic acid copolymer nanoparticles: A small-angle X-ray scattering study using direct Fourier and indirect maximum-entropy methods. Journal of Applied Crystallography, 28, 774-781.

Potton Daniell, GJ, and Melville, D (1988a) A new method for the determination of particle-size distribu-tions from small-angle neutron-scattering measurements. Journal of Applied Crystallography, 21, 891-897.

Potton, JA, Daniell, GJ, and Rainford, BD (1988b) Particle size distributions from SANS data using the maximum entropy method. *Journal of Applied Crystallography*, **21**, 663-668.

Radlinski, A.P. (2006) Small-angle neutron scattering and rock microstructure. In: Neutron Scattering in Earth Sciences, ed. by H.-R. Wenk, Reviews in Mineralogy and Geochemistry 63, 363-397.

Radlinski, AP, Ioannidis, MA, Hinde, AL, Hainbuchner, M, Baron, M, Rauch, H, and Kline, SR (2004) Angstrom-to-millimeter characterization of sedimentary rock microstructure. J. Colloid Interface Sci. 274, 607-612.

Rother G, Melnichenko YB, Cole DR Frielinghaus H, and Wignall GD (2007) Microstructural characterization of adsorption and depletion regimes of supercritical fluids in nanopores J. Phys. Chem. C. 111, 15736-15742.